

Prediction of the spin triplet two-electron quantum dots in Si: towards controlled quantum simulations of magnetic systems

D. Miserev

Department of Physics, University of Basel, Klingelbergstrasse 82, CH-4056 Basel, Switzerland

O. P. Sushkov

School of Physics, University of New South Wales, Sydney, Australia

(Dated: August 8, 2019)

Ground state of two-electron quantum dots in single-valley materials like GaAs is always a spin singlet regardless of what the potential and interactions are. This statement cannot be generalized to the multi-valley materials like n -doped Si. Here we calculate the spectrum of a two-electron Si quantum dot analytically and numerically and show for the first time that the dot with the lateral size of several nm can have the spin triplet ground state which is impossible in the single-valley materials. Predicted singlet-triplet level crossing in two-electron Si quantum dots can potentially establish the platform for quantum simulation of magnetic many-body systems based on the triplet quantum dots. We suggest several examples of such systems that open a way to controlled quantum simulations within the condensed matter setting.

I. INTRODUCTION

Electrons in Si have the valley degree of freedom¹ which makes them qualitatively different from electrons in atoms or in one-valley materials. In this paper we concentrate on properties of two-electron bound states in Si. In atomic physics the ground state of two bound electrons is always a spin singlet. This is a general property that is independent of potential well and interaction². The proof of this statement is based on that the ground state wave function in one-valley materials must have no nodes. This is no longer valid for multi-valley electrons such as electrons in Si, whose ground state wave functions can have arbitrary number of nodes. In this paper we, for the first time, predict the regime when the ground state of a tunable two-electron Si quantum dot is the spin triplet.

Tunable quantum dots are typically built in heterostructures where the potential along the z axis is presented by the layer edges and is much stronger than the lateral (x, y) potential that is controlled by the electrostatic gates. Tunneling between valleys lifts the valley degeneracy^{3,4}. Theoretical calculation of the single-electron valley splitting ω_0 is itself a nontrivial tunneling problem⁵ that is very sensitive to the interface potential⁶. The effect of Coulomb interaction in few electron Si quantum dots has been considered previously⁷. The conclusion of Ref.⁷ was that the inter-valley Coulomb exchange effects are negligible for any size of the quantum dot. Hence the ground state of a two-electron dot in Si is always a spin singlet. Here we revisit this problem and predict values of the exchange matrix element by 2–3 orders of magnitude higher than that obtained in Ref.⁷. This makes a qualitative difference on the role of exchange Coulomb interaction. In particular, at the lateral size of a quantum dot smaller than several nm the exchange Coulomb interaction becomes larger than the valley splitting ω_0 which experimental range is $\omega_0 \sim 0.1 - 1.5$ meV,

see Refs.^{4,8,9}. This results in the triplet ground state which is a new physical phenomenon that has never been predicted before.

The singlet-triplet level crossing can be driven by the electrostatic gates⁹ controlling the quantum dot size and thus changing the ratio between the single-electron valley splitting ω_0 and the exchange Coulomb matrix element. The tunable singlet-triplet level crossing can be used to create artificial multi-dot magnetic systems which exhibit strongly correlated many-body physics with externally driven quantum phase transitions. The spirit of this idea is similar to quantum simulations of the Mott-Hubbard model in arrays of quantum dots^{10–12}. However, absence of the charge dynamics in spin systems makes them almost insensitive to the Coulomb disorder¹³ which significantly reduces requirements to the quality of nanofabrication. The local spin measurements can be already done with the help of spin-polarized scanning tunneling microscopy^{14–16}. To be specific, we discuss Haldane spin 1 chain¹⁷, the topological spin 1/2 edge states¹⁸, and the quantum phase transition from Haldane chain to the “antiferromagnetic spin ladder”¹⁹. We also discuss $O(3)$ quantum criticality in square arrays²⁰ and underline quantum criticality in triangular arrays where the nature of quantum phase transition is not clearly understood theoretically.

Our paper is organized as follows. In Sec. II, we provide the theoretical model describing two-electron Si quantum dot. In Sec. III, we calculate the exchange Coulomb matrix element within the effective mass approximation. In Sec. IV, we calculate the Coulomb matrix elements exactly using the tight-binding electron wave function. The resulting low-energy spectrum of the two-electron quantum dot is presented in Sec. V. Possible applications of the triplet quantum dots for quantum simulations of the 1D and 2D spin-1 systems are proposed in Sec. VI. Conclusions are given in Sec. VII.

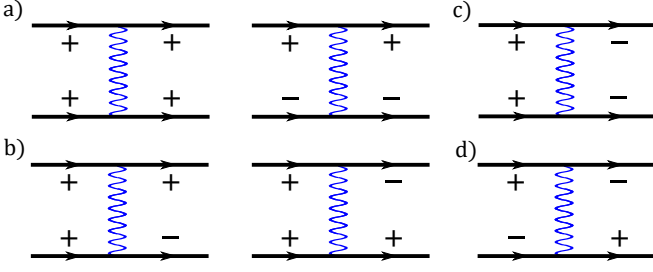


FIG. 1. Matrix elements of the Coulomb interaction Eq. (3), \pm indicates the valley: (a) direct Coulomb diagrams; (b) diagrams with the total momentum change $\Delta q_z = \pm 2q_0$; (c) diagrams with the total momentum change $\Delta q_z = \pm 4q_0$; (d) the exchange Coulomb diagram. Other diagrams can be obtained from the presented ones by changing signs of all valleys and/or complex conjugation.

II. THEORETICAL MODEL

We describe electron dispersion along the $z = [001]$ direction using one-dimensional (1D) tight binding model suggested in Ref.²¹. In order to reproduce two degenerate minima of the Si dispersion along the z direction, one has to account for the nearest and next-to-nearest neighbor hopping terms given by the matrix elements v and u , respectively:

$$H_z = \sum_{i_z, \sigma=\uparrow, \downarrow} \left\{ v c_{i_z, \sigma}^\dagger c_{i_z+1, \sigma} + u c_{i_z, \sigma}^\dagger c_{i_z+2, \sigma} + h.c. + (V(i_z) + \varepsilon_0) c_{i_z, \sigma}^\dagger c_{i_z, \sigma} \right\}. \quad (1)$$

Here $c_{i_z, \sigma}^\dagger$ is the electron creation operator at the site i_z with the spin projection σ , $V(i_z)$ is the heterostructure interface potential. The constant ε_0 is chosen to set the dispersion minimum at $\varepsilon = 0$. The corresponding dispersion of free electrons is then the following:

$$\varepsilon(q) = \varepsilon_0 + 2v \cos(qb) + 2u \cos(2qb), \quad (2)$$

where $b = 1.36 \text{ \AA}$ is the inter-atomic spacing along the z axis, $-\pi/b < q < \pi/b$ is the unfolded Brillouin zone (BZ). We take parameters $v \approx 0.68 \text{ eV}$, $u \approx 0.61 \text{ eV}$ from Ref.²¹ as they fit the Si dispersion the best. The minima of dispersion are located at $\pm q_0$, $q_0 \approx 0.59 \pi/b$.

The description in Ref.²¹ is based on the folded BZ while here we use the unfolded BZ. In the “unfolded description” the free electron wave function is a simple plane wave and therefore this description is more convenient for calculations of Coulomb matrix elements. The relation between “folded” and “unfolded” descriptions is considered in Appendix A, where we also explain why our value of the exchange interaction is by orders of magnitude larger than that of Ref.⁷.

The lateral size of a quantum dot is determined by electrostatic gates. As the valley splitting ω_0 is much smaller than the lateral level spacing, the lateral wave function $\phi(\mathbf{r})$, $\mathbf{r} = b(i_x, i_y)$, can be taken the same for the lowest

valley split states. The actual lateral wave function is not important and for numerical calculations we model it by the Gaussian such that the dot size D is defined through the inverse participation ratio, see Eq. (9).

Finally, we introduce the electron-electron interaction:

$$H_C = U_H \sum_i c_{i\uparrow}^\dagger c_{i\downarrow}^\dagger c_{i\downarrow} c_{i\uparrow} + \frac{1}{2} \sum_{\substack{i \neq j \\ \alpha, \beta}} V_{ij} c_{i\alpha}^\dagger c_{j\beta}^\dagger c_{j\beta} c_{i\alpha}, \quad (3)$$

where $\alpha, \beta = \uparrow, \downarrow$ are spin indexes, $i = (i_x, i_y, i_z)$ enumerates the lattice sites, U_H is the on-site Hubbard interaction and V_{ij} is the long range Coulomb interaction:

$$V_{ij} = \frac{V_0}{\sqrt{(i_x - j_x)^2 + (i_y - j_y)^2 + (i_z - j_z)^2}}, \quad (4)$$

where $V_0 = e^2/\epsilon b$ is the electron-electron interaction at nearest sites, e is the electron charge, ϵ is the dielectric constant. In this paper we use the Coulomb parameters calculated in Ref.²² via DFT+U+V method: $U_H \approx 3.5 \text{ eV}$, $V_0 \approx 1.35 \text{ eV}$.

III. EFFECTIVE MASS APPROXIMATION

First, we estimate the exchange Coulomb matrix elements analytically using the continuous effective mass approximation (EMA). The quantum dot has a pancake shape of thickness $d \sim 1 \text{ nm}$ and the lateral size D , $d \ll D$. This geometry is realistic and such a small thickness d is required to obtain the sizable single-electron valley splitting ω_0 , e.g. see Ref.⁹. As $d \ll D$, the single-electron wave function can be factorized $\psi(z, \mathbf{r}) = \varphi(z)\phi(\mathbf{r})$, where $\mathbf{r} = (x, y)$. Within the EMA approximation we can work in the basis of valley states

$$|\pm\rangle = \varphi_\pm(z) = e^{\pm i q_0 z} \Phi(z), \quad (5)$$

where $\Phi(z)$ is the smooth envelope satisfying the Schrödinger equation:

$$\left(\frac{\hat{p}_z^2}{2m^*} + V(z) \right) \Phi(z) = E_0 \Phi(z). \quad (6)$$

Here $V(z)$ is the interface potential, $\hat{p}_z = -i\partial_z$ is the momentum operator along the z axis, $m^* \approx 0.92m$ is the effective mass, E_0 is the ground state energy.

The continuous limit is only applicable when two valleys are close i.e. $q_0 \ll \pi/b$. However, in Si $q_0 \approx 0.59 \pi/b$, so the valley separation Eq. (5) is questionable. Further we provide exact numerical solution that does not require the continuous limit as well as the valley separation (5), but we believe that this simple analytical estimate provides an important insight to the problem. In the valley basis the single-particle Hamiltonian (1) has only off-diagonal matrix elements

$$\langle + | H_z | - \rangle = \langle - | H_z | + \rangle = \frac{\omega_0}{2}, \quad (7)$$

where ω_0 is the single-electron valley splitting.

Two-electron matrix elements of the Coulomb interaction are presented in Fig. 1. The direct diagrams in Fig. 1(a) yield the same value and do not contribute to the two-electron level splitting. The diagrams where only one electron changes the valley index, Fig. 1(b), are exponentially suppressed $\sim e^{-2q_0 d}$ due to the large difference $\Delta q_z = \pm 2q_0$ between total initial and final momenta, see Appendix B. In the limit $q_0 d \gg 1$ we neglect them. The diagram in Fig. 1(c) corresponding to processes where the total momentum q_z is changed from $2q_0$ to $-2q_0$ is doubly exponentially suppressed $\sim e^{-4q_0 d}$ and we neglect it. The last diagram, Fig. 1(d), corresponds to the intervalley exchange scattering which is responsible for the singlet-triplet level crossing in two-electron Si quantum dots.

The Hubbard contribution to the exchange diagram, Fig. 1(d), within the EMA reads:

$$M_{ex}^{(H)} = U_H b^3 \int \Phi^4(z) \phi^4(\mathbf{r}) dz d\mathbf{r} = U_H \frac{b^3}{d D^2}, \quad (8)$$

where we introduced the lateral size of the quantum dot D and the Si layer width d via the inverse participation ratios:

$$\frac{1}{d} = \int \Phi^4(z) dz, \quad \frac{1}{D^2} = \int \phi^4(\mathbf{r}) d\mathbf{r}. \quad (9)$$

The long-range Coulomb part of the interaction can be calculated analytically in the limit $q_0 d \gg 1$, see Appendix B:

$$M_{ex}^{(V)} \approx \frac{\pi V_0 b}{q_0^2} \int \Phi^4(z) \phi^4(\mathbf{r}) dz d\mathbf{r} = \frac{\pi V_0}{(q_0 b)^2} \frac{b^3}{d D^2}. \quad (10)$$

Both Coulomb matrix elements, (8) and (10), scale as $\propto 1/dD^2$ or equivalently, as $1/N_Q$, where N_Q is total number of Si atoms in the quantum dot. For a dot with $d = 1$ nm and $D = 4$ nm we obtain the following value of the exchange Coulomb matrix element in meV:

$$M_{ex} = M_{ex}^{(H)} + M_{ex}^{(V)} \approx 4.73(eV) \frac{b^3}{d D^2} \approx 0.74. \quad (11)$$

This value is by more than two orders of magnitude larger than that from Ref.⁷ (with appropriate dot size scaling) and it is comparable with the observed single electron valley splitting ω_0 ^{8,9}. In order to obtain the sizable exchange Coulomb matrix element (11), we need the lateral size D of the quantum dot to be sufficiently small, namely $D \lesssim 5$ nm. We argue that it is realistic because gate defined $D \approx 10$ nm quantum dots are already possible, e.g. see Ref.⁹.

IV. EXACT COULOMB MATRIX ELEMENTS

To support our analytical estimates, we present exact numerical solution of the problem. First, we calculate the single electron valley splitting ω_0 for three different shapes of the interface potential: rectangular, parabolic

TABLE I. Energies of four lowest states and the ground state splitting $\omega_0 = \varepsilon_2 - \varepsilon_1$ (given in meV) for different shapes of the interface potential. The size of the ground state in all cases is $d = 1$ nm.

shape	ε_1	ε_2	ε_3	ε_4	ω_0
rectangular	73.87	85.79	287.10	317.61	11.93
parabolic	105.08	105.08	310.64	310.64	6×10^{-9}
δ -doping	110.22	110.52	321.18	321.21	0.30

TABLE II. Nonzero Coulomb matrix elements M_{abcd} (meV) for rectangular, parabolic and δ -doped interface potentials. The dot lateral size is $D = 4$ nm, the Si layer width $d = 1$ nm. We present the Hubbard, U_H , and the long-range Coulomb contributions, V , see Eq. (3), as well as their sum. For direct matrix elements we also present their values with subtracted charging energy $U_C = M_{1122}$.

	M_{1111}	M_{2222}	M_{1122}	M_{1212}
rectangular				
V	115.92	117.40	116.52	0.26
U_H	0.52	0.56	0.18	0.18
$V + U_H$	116.44	117.96	116.70	0.44
$V + U_H - U_C$	-0.27	1.26	0	
parabolic				
V	115.96	115.96	115.84	0.06
U_H	0.54	0.54	0.17	0.17
$V + U_H$	116.50	116.50	116.01	0.23
$V + U_H - U_C$	0.49	0.49	0	
δ -doping				
V	116.25	116.23	116.12	0.06
U_H	0.55	0.55	0.18	0.18
$V + U_H$	0.80	0.78	0.30	0.24
$V + U_H - U_C$	0.50	0.48	0	

and parabolic with δ -doping. In the latter case we model the impurity-doped monolayer by a positively charged plane creating the potential $\delta V(i_z) = e\alpha b|i_z|$, where α is the electric field created by the charged plane. For further calculations we choose $\alpha = 15.4$ meV/nm. All interface potentials are chosen such that the inverse participation ratio $d = 1$ nm in all cases. Energies of four lowest states as well as the ground state splitting ω_0 are shown in Table I. The ground state splitting for the rectangular well is large, $\omega_0 \sim 10$ meV, while for the parabolic well ω_0 is practically zero. This illustrates the well-known result that ω_0 appears due to the sharp interface^{5,6}. The moderate δ -doping allows to obtain intermediate values of ω_0 that are consistent with the experiments^{4,8,9}. For example, the chosen value of $\alpha = 15.4$ meV/nm is sufficient to give $\omega_0 = 0.3$ meV.

Using exact eigenfunctions of the Hamiltonian Eq. (1), we calculate the interaction matrix elements M_{abcd} , for different interface potentials, see Table II. Indexes $a, b, c, d \in \{1, 2\}$ label first two single electron states that are split by ω_0 , see Table I. In the notation M_{abcd} the

state a scatters to b and the state c scatters to d . The dot lateral size is $D = 4$ nm. Direct matrix elements M_{1111} , M_{2222} , and M_{1122} are large because they contain the charging energy $U_C \equiv M_{1122} \approx 116$ meV. The charging energy does not influence the level order, therefore in Table II we also present values of the direct matrix elements with subtracted U_C . As we see from Table II, the Coulomb matrix elements are very weakly sensitive to the potential shape unlike the single-electron splitting ω_0 which varies by several orders of magnitude, see Table I. This is because ω_0 results from the inter-valley tunneling which is especially strong for sharp interfaces. The Coulomb matrix elements are in turn not sensitive to the details of interface and fully defined by the quantum dot geometry, see Eqs. (8), (10). From the relation $M_{ex} \approx 2M_{1212}$, see Appendix B, and Table II it follows that $M_{ex} \approx 0.5$ meV, which is close to the crude analytical estimate (11).

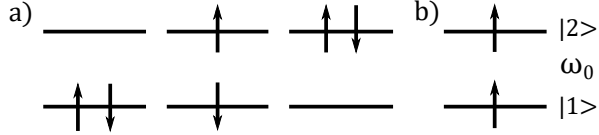


FIG. 2. Lowest energy levels of a two-electron Si quantum dot: (a) three spin singlets; (b) the spin triplet (other two projections are not shown). Here $|1\rangle$, $|2\rangle$ are two lowest one-particle states that are separated by the single-particle valley splitting ω_0 , see Table I.

V. LOW-ENERGY SPECTRUM OF TWO-ELECTRON QUANTUM DOT

The low-energy spectrum of a two-electron Si quantum dot consists of three spin singlets with the orbital wave functions $|1\rangle|1\rangle$, $|2\rangle|2\rangle$, $\frac{1}{\sqrt{2}}[|1\rangle|2\rangle + |2\rangle|1\rangle]$ and the triplet with the orbital wave function $\frac{1}{\sqrt{2}}[|1\rangle|2\rangle - |2\rangle|1\rangle]$, where $|1\rangle$ and $|2\rangle$ are two lowest valley-split states, see Fig. 2. In given basis, the singlet channel is described by the following effective Hamiltonian:

$$H_S = \begin{pmatrix} M_{1111} - \omega_0 & M_{1212} & 0 \\ M_{1212} & M_{2222} + \omega_0 & 0 \\ 0 & 0 & M_{1122} + M_{1212} \end{pmatrix}. \quad (12)$$

Diagonalizing H_S , we find the energy E_S of the lowest singlet:

$$E_S = \frac{M_{1111} + M_{2222}}{2} - \sqrt{M_{1212}^2 + (\omega_0 - \gamma)^2}, \quad (13)$$

where $\gamma = (M_{1111} - M_{2222})/2$. The triplet state energy reads:

$$E_T = M_{1122} - M_{1212}. \quad (14)$$

If $E_T < E_S$, then the triplet state is the ground state of a two-electron quantum dot. It yields the condition for

ω_0 :

$$\omega_0 < \omega^* = \gamma + \sqrt{\delta^2 - M_{1212}^2}, \quad (15)$$

where $\delta = M_{1212} + (M_{1111} + M_{2222} - 2M_{1122})/2$. For the rectangular interface potential $\omega^* \approx 0.06$ meV which is much smaller than the valley splitting $\omega_0 \approx 12$ meV, so the ground state in this case is the spin singlet. However, for the parabolic and the δ -doping models $\omega^* \approx 0.7$ meV i.e. the ground state here is the spin triplet as $\omega_0 < \omega^*$, see Table I.

VI. QUANTUM SIMULATIONS OF MAGNETIC SYSTEMS BASED ON THE TRIPLET QUANTUM DOTS

We further propose to use the triplet Si quantum dots as building blocks for simulation of quantum magnetic systems. Consider first a pair of two-electron quantum dots shown schematically in Fig. 3. The electron density

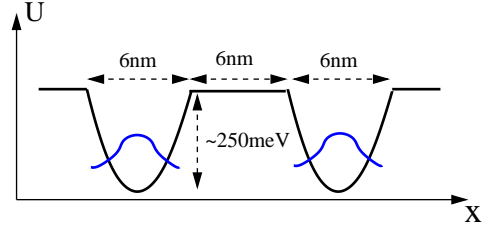


FIG. 3. Schematic double dot setup.

shown by blue lines has width $D = 4$ nm. In absence of interaction this requires the depth of the lateral potential ~ 100 meV. Taking into account the charging energy $U_C = M_{1122} \approx 116$ meV, see Table II, the depth of quantum dot potential should be at least 200 – 250 meV in order to accommodate two electrons. The size of the electron wave function D is controlled by the lateral gates and can drive the singlet-triplet level crossing inside the quantum dot. This allows us to consider a quantum dot as an effective site that can have spin zero, $S = 0$, in the singlet state or spin one, $S = 1$, in the triplet state. Let us also denote the on-site energy splitting $E_T - E_S$ as Δ , where E_T (E_S) is the energy of the lowest triplet (singlet) state, see Eqs. (13), (14). Interaction between spins $\mathbf{S}_{1,2}$ in different quantum dots is due to the antiferromagnetic Anderson superexchange²³:

$$H_J = J \mathbf{S}_1 \cdot \mathbf{S}_2, \quad J = \frac{4t^2}{U_C}, \quad (16)$$

where $U_C \approx 116$ meV is the charging energy, t is the tunneling matrix element between the dots. Nontrivial many-body regime in an array of dots corresponds to $J \sim \omega^* \sim \omega_0 \sim 1$ meV, ω^* is given in Eq. (15). It yields an estimate for the tunneling matrix element $t \approx 5$ meV which corresponds to the distance between the dots $R = 10 - 15$ nm. Value of J is independently controllable by

the depth of the quantum well, see Fig. 3. Variation of the depth from 250 meV to 300 meV is changing J by several times.

Spin states of the single dot, $S = 0, 1$, can be described by a spin dimer consisting of two spins $1/2$ with Hamiltonian $H_d = \Delta(\mathbf{s}_1 \cdot \mathbf{s}_2)$, $s_1 = s_2 = 1/2$, $\Delta = E_T - E_S$. Nearest dimers interact antiferromagnetically, Eq. (16). Hence, using the bond operator representation²⁴, the array of dots can be mapped to an array of spin $1/2$ dimers. It is well known that arrays of spin dimers manifest very rich many body physics. Here we point out only three specific examples illustrated in Fig. 4.

Consider first 1D array, Fig. 4(a). If $\Delta < 0$ and

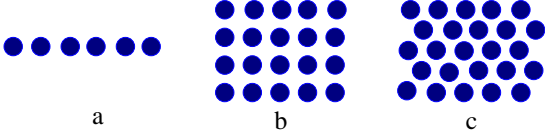


FIG. 4. Linear (a), square (b), and triangular (c) lattices of quantum dots.

$|\Delta| \gtrsim J$, the array represents Haldane spin chain¹⁷, and hence, the topological spin $1/2$ edge states¹⁸ can be observed experimentally. Increasing Δ , $\Delta \rightarrow +0$, one drives the Haldane chain through the quantum phase transition to the “antiferromagnetic spin ladder”. This would allow to observe fractionalization of spin excitations at the transition¹⁹.

The 2D array of tunable dots (spin dimers) on square lattice, Fig. 4(b), manifests the $O(3)$ quantum critical physics driven by variation of Δ , see e.g. Ref.²⁰. This physics is well understood theoretically, but experimentally it has been observed only in 3D spin-dimerized compounds^{25,26}. The 2D $O(3)$ physics is different and it has never been observed experimentally.

The 2D array on triangular lattice, Fig. 4(c), is especially interesting. If $\Delta < 0$ and $|\Delta| \gtrsim J$, this is the spin 1 antiferromagnet on the triangular lattice. Increasing Δ , $\Delta \rightarrow +0$, must drive the system to the quantum disordered state. Such an experiment can shed the light on the nature of this quantum phase transition which is not clearly understood theoretically.

VII. CONCLUSIONS

In conclusion, we predict theoretically the singlet-triplet level crossing in two-electron Si quantum dots. This phenomenon is especially remarkable as such a level crossing is not possible in single-valley materials². The level crossing can be controlled by electrostatic gates. It opens opportunity for controlled quantum simulations of magnetic systems where single magnetic site is given by a triplet quantum dot. Here we suggest to simulate 1D spin systems (e.g. Haldane spin 1 chain hosting topological spin $1/2$ edges states) and 2D arrays of quantum

dots that are expected to have rich critical phenomena not yet observed experimentally.

Acknowledgments. We thank Dimitrie Culcer, Susan Coppersmith, Andre Saraiva, Joe Salfi, and Alexander Yaresko for very important stimulating discussions. D.M and O.P.S acknowledge support of the Australian Research Council Centre of Excellence in Future Low-Energy Electronics Technologies (project number CE170100039) and funded by the Australian Government. D.M acknowledges support of the Georg H. Endress foundation.

Appendix A: FOLDED AND UNFOLDED BRILLOUIN ZONES

Eigenstates of the 1D Hamiltonian Eq. (1) are plane waves:

$$|q\rangle = \frac{1}{\sqrt{2N}} \sum_{i_z} e^{iqbi_z} c_{i_z}^\dagger |0\rangle \quad (\text{A1})$$

with the spectrum (2), $2N$ is the total number of Si atoms in the chain. Two minima of the dispersion correspond to $\pm q_0$, $q_0 = \arccos(-v/4u)/b \approx 0.59\pi/b$. This is the “unfolded” description, see Fig. 6.

We could alternatively consider the Si chain with the elementary cell consisting of two atoms, such that new lattice spacing is $a = 2b = 2.7 \text{ \AA}$, see Fig. 5. The wave function that accounts for the unit cell structure is then the following:

$$|k\rangle = \frac{1}{\sqrt{N}} \sum_{i_z} e^{ikai_z} \left(\alpha \xi_{i_z}^\dagger + \beta \eta_{i_z}^\dagger \right) |0\rangle, \quad (\text{A2})$$

where $\xi_{i_z}^\dagger = c_{2i_z}^\dagger$ ($\eta_{i_z}^\dagger = c_{2i_z+1}^\dagger$) is the electron creation operator at the “circle” (“square”) cite of the lattice, see Fig. 5. N is the total number of unit cells in the lattice. The corresponding dispersion $\varepsilon_\pm(k)$ and the Bloch amplitudes $\mathcal{B}_\pm(k)$ are the following²¹:

$$\varepsilon_\pm(k) = \varepsilon_0 + 2u \cos(ka) \pm 2v \cos(ka/2), \quad (\text{A3})$$

$$\mathcal{B}_\pm(k) = \begin{pmatrix} \alpha \\ \beta \end{pmatrix} = \frac{1}{\sqrt{2}} \begin{pmatrix} 1 \\ \pm e^{ika/2} \end{pmatrix}. \quad (\text{A4})$$

This is the “folded” description, see Fig. 6. Here we use quasimomentum k for the “folded” case, $-\pi/a < k < \pi/a$ and q for the “unfolded” case, $-\pi/b < q < \pi/b$.

$\varepsilon_-(k)$ corresponds to the lower branch of dispersion, see Fig. 6. Minima of $\varepsilon_-(k)$ are at $\pm k_0$, $k_0 = 2 \arccos(v/4u)/a \approx 0.82\pi/a$. The corresponding wave function (A2) can be written as

$$\psi_-(z) = e^{ikz} \mathcal{B}_-(k), \quad (\text{A5})$$

where $\mathcal{B}_-(k)$ is the Bloch amplitude, Eq. (A4). The overlap of Bloch amplitudes corresponding to two minima of the dispersion is then the following:

$$|\mathcal{B}_-^\dagger(-k_0) \cdot \mathcal{B}_-(k_0)| = \cos\left(\frac{k_0 a}{2}\right) = \frac{v}{4u} \approx 0.28. \quad (\text{A6})$$

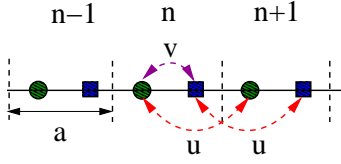


FIG. 5. 1D model for the two valley z -dispersion in Si interface²¹. There are two Si atoms in the elementary cell. The lattice spacing is $a = 2b = 2.7 \text{ \AA}$, v and u are the nearest and next-to-nearest neighbor hoppings, respectively.

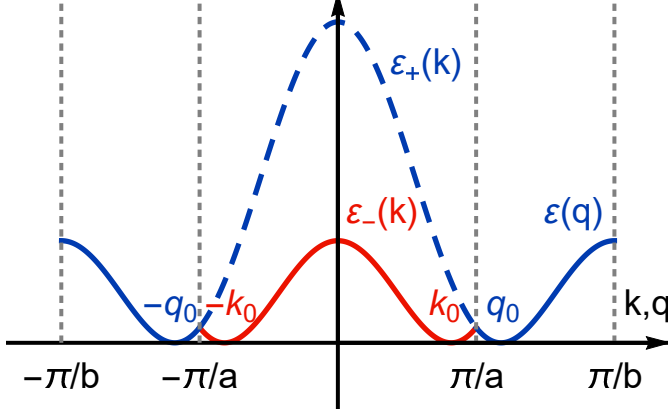


FIG. 6. The “unfolded” and “folded” dispersions Eqs. (2), (A3). Gray dotted lines show the “unfolded” $-\pi/b < q < \pi/b$ and “folded” $-\pi/a < k < \pi/a$ Brillouin zones, $a = 2b$. The branch $\varepsilon_+(k)$ coincides with the “unfolded” dispersion $\varepsilon(q)$ (indicated by the dashed blue line). The branch $\varepsilon_-(k)$ (the red line) is the mirror image of the rest of $\varepsilon(q)$ (the solid blue line). $\pm q_0$ ($\pm k_0$) are the dispersion minima corresponding to the “unfolded” (“folded”) description.

In this paper we use the “unfolded” description as it does not involve the Bloch amplitudes Eq. (A4). However, in Ref.⁷ the “folded” description was used. The overlap of Bloch functions corresponding to different valleys, Eq. (A6), was largely underestimated in Ref.⁷. This is the main reason why our result for the exchange Coulomb matrix element is more than two orders of magnitude higher than that in Ref.⁷ (with the appropriate dot size scaling).

Appendix B: ANALYTIC ESTIMATE OF THE EXCHANGE INTEGRAL

Here we take the continuous limit and use the effective mass approximation (EMA) to calculate the electron wave function $\psi(z, \mathbf{r})$. It is convenient to work in the valley basis, see Eq. (5). Coulomb matrix elements, see Fig. 1, consist of the Hubbard and the long-range

part. The long-range Coulomb part reads:

$$M_{\mu\mu'\nu\nu'}^{(V)} = \frac{e^2}{\epsilon} \int \frac{e^{iq_0(\mu-\mu')z_1} e^{iq_0(\nu-\nu')z_2}}{\sqrt{(z_1-z_2)^2 + (\mathbf{r}_1-\mathbf{r}_2)^2}} \Phi^2(z_1)\Phi^2(z_2)\phi^2(\mathbf{r}_1)\phi^2(\mathbf{r}_2) dz_1 dz_2 d\mathbf{r}_1 d\mathbf{r}_2, \quad (\text{B1})$$

where $\mu, \nu = \pm 1$ ($\mu', \nu' = \pm 1$) are valley indexes of the initial (final) states, ϵ is the dielectric constant. The Hubbard part is especially simple due to its short-range nature:

$$M_{\mu\mu'\nu\nu'}^{(H)} = U_H b^3 \int e^{iq_0(\mu+\nu-\mu'-\nu')z} \Phi^4(z) \phi^4(\mathbf{r}) dz d\mathbf{r} \quad (\text{B2})$$

In the limit $q_0 d \gg 1$ the Hubbard matrix elements with $\mu + \nu - \mu' - \nu' \neq 0$ are negligible due to the quickly oscillating exponential factor. Therefore, we only consider $M_{\mu\mu'\nu\nu'}^{(H)}$ that conserve total valley quantum number i.e. $\mu + \nu - \mu' - \nu' = 0$, see Fig. 1(a),(d). All such matrix elements take the same value $M_{ex}^{(H)} = U_H b^3 / d D^2$ presented in Eq. (8), d and D are defined through the inverse participation ratios, see Eq. (9).

The long-range part of Eq. (B1) is a bit trickier. In order to evaluate it, we use the momentum representation. We define the Fourier transform of the lateral electron density:

$$\rho(\mathbf{q}) = \int \phi^2(\mathbf{r}) e^{-i\mathbf{q}\cdot\mathbf{r}} d^2r. \quad (\text{B3})$$

Using $\rho(\mathbf{q})$, we can rewrite Eq. (B1) as follows:

$$M_{\mu\mu'\nu\nu'}^{(V)} = \frac{e^2}{\epsilon} \int \frac{2\pi}{q} |\rho(\mathbf{q})|^2 v(q) \frac{d\mathbf{q}}{(2\pi)^2}, \quad v(q) = \int dz_1 dz_2 e^{iq_0(\mu-\mu')z_1} e^{iq_0(\nu-\nu')z_2} e^{-q|z_1-z_2|} \Phi^2(z_1) \Phi^2(z_2). \quad (\text{B4})$$

Using the Fourier transform of the quantum well electron density

$$R(k) = \int \Phi^2(z) e^{-ikz} dz, \quad (\text{B5})$$

one can represent the form-factor $v(q)$ in the following form:

$$v(q) = q \int \frac{R(k) R^*(k + q_0(\mu + \nu - \mu' - \nu'))}{q^2 + (k + (\mu - \mu')q_0)^2} \frac{dk}{\pi}. \quad (\text{B6})$$

Eq. (B6) is exact. Notice again that if $\mu + \nu - \mu' - \nu' \neq 0$, then the function under the integral Eq. (B6) is small everywhere because $R(k)$ is non-zero at $|k| \lesssim 1/d$ (uncertainty principle) and $q_0 \gg 1/d \sim |k|$. Therefore, only the diagrams with $\mu + \nu - \mu' - \nu' = 0$ contribute, see Fig. 1(a),(d). The diagrams in Fig. 1(a) correspond to $\mu = \mu', \nu = \nu'$ and give the direct Coulomb matrix elements that are all equal and do not influence the level ordering in a two-electron quantum dot. The diagram in Fig. 1(d) is the exchange Coulomb interaction which corresponds to $\mu - \mu' = \pm 2$:

$$v_{ex}(q) = q \int_{-\infty}^{\infty} \frac{|R(k)|^2}{q^2 + (k \pm 2q_0)^2} \frac{dk}{\pi}. \quad (\text{B7})$$

In the limit $q_0 d \gg 1$ we can neglect k -dependence and q -dependence in the denominator as $k \lesssim 1/d \ll q_0$ and $q \lesssim 1/D \ll 1/d \ll q_0$:

$$v_{ex}(q) \approx \frac{2q}{(2q_0)^2} \int |R(k)|^2 \frac{dk}{2\pi} = \frac{q}{2q_0^2} \int \Phi^4(z) dz. \quad (B8)$$

Substituting $v_{ex}(q)$ into Eq. (B4), we get the estimate for the long-range contribution to the exchange Coulomb matrix element presented in Eq. (10):

$$M_{ex}^{(V)} \approx \frac{\pi e^2}{\epsilon q_0^2} \int \Phi^4(z) \phi^4(\mathbf{r}) dz d\mathbf{r} = \frac{\pi V_0}{(q_0 b)^2} \frac{b^3}{d D^2}, \quad (B9)$$

where $V_0 = e^2/\epsilon b$ is the Coulomb repulsion at nearest sites.

We cannot compare directly the matrix element $M_{ex} = M_{ex}^{(H)} + M_{ex}^{(V)}$ with the numerical calculations because the valley wave functions, Eq. (5), are not exact single-electron eigenfunctions due to the valley splitting ω_0 . True wave functions are some linear combinations of the valley wave functions (5). In case of symmetric interface potential $V(-z) = V(z)$ the true wave function must also be symmetric or anti-symmetric, so the good basis is $|1\rangle = \sqrt{2} \cos(q_0 z)$, $|2\rangle = \sqrt{2} \sin(q_0 z)$ instead of $|\pm\rangle = e^{\pm i q_0 z}$ used above. Using the linearity, one can represent the matrix elements M_{abcd} , $a, b, c, d \in \{1, 2\}$, in the new basis through the matrix elements in the valley basis. In the matrix element M_{abcd} the state a (c) scatters to the state b (d). In particular, $M_{1212} = M_{ex}/2$ which is used to compare the numerical result with the analytical estimate.

-
- ¹ F. A. Zwanenburg, A. S. Dzurak, A. Morello, M. Y. Simmons, L. C. L. Hollenberg, G. Klimeck, S. Rogge, S. N. Coppersmith, and M. A. Eriksson, *Rev. Mod. Phys.* **85**, 961 (2013).
 - ² N. W. Ashcroft, and N. D. Mermin, *Solid State Physics*, Saunders, New York, 1974.
 - ³ M. G. Borselli, R. S. Ross, A. A. Kiselev, E. T. Croke, K. S. Holabird, P. W. Deelman, L. D. Warren, I. Alvarado-Rodriguez, I. Milosavljevic, F. C. Ku, W. S. Wong, A. E. Schmitz, M. Sokolich, M. F. Gyure, and A. T. Hunter, *Appl. Phys. Lett.* **98**, 123118 (2011).
 - ⁴ S. Goswami, K. A. Slinker, M. Friesen, L. M. McGuire, J. L. Truitt, C. Tahan, L. J. Klein, J. O. Chu, P. M. Mooney, D. W. van der Weide, R. Joynt, S. N. Coppersmith, and M. A. Eriksson, *Nat. Phys.* **3**, 41 (2007).
 - ⁵ A. L. Saraiva, M. J. Caldern, R. B. Capaz, X. Hu, S. Das Sarma, and B. Koiller, *Phys. Rev. B* **84**, 155320 (2011).
 - ⁶ A. L. Saraiva, M. J. Caldern, X. Hu, S. Das Sarma, and B. Koiller, *Phys. Rev. B* **80**, 081305(R) (2009).
 - ⁷ L. Jiang, C. H. Yang, Z. Pan, A. Rossi, A. S. Dzurak, and D. Culcer, *Phys. Rev. B* **88**, 085311 (2013).
 - ⁸ T. Ando, A. B. Fowler, and F. Stern, *Rev. Mod. Phys.* **54**, 437 (1982).
 - ⁹ C. H. Yang, A. Rossi, R. Ruskov, N. S. Lai, F. A. Mohiyaddin, S. Lee, C. Tahan, G. Klimeck, A. Morello and A. S. Dzurak, *Nat. Commun.* **4**, 2069 (2013).
 - ¹⁰ A. Singha, M. Gibertini, B. Karmakar, S. Yuan, M. Polini, G. Vignale, M. I. Katsnelson, A. Pinczuk, L. N. Pfeiffer, K. W. West, V. Pellegrini, *Science* **332**, 1176 (2011).
 - ¹¹ J. Salfi, J. A. Mol, R. Rahman, G. Klimeck, M. Y. Simmons, L. C. L. Hollenberg, and S. Rogge, *Nat. Commun.* **7**, 11342 (2016).
 - ¹² T. Hensgens, T. Fujita, L. Janssen, X. Li, C. J. Van Diepen, C. Reichl, W. Wegscheider, S. Das Sarma, and L. M. K. Vandersypen, *Nature* **548**, 70 (2017).
 - ¹³ O. A. Tkachenko, V. A. Tkachenko, I. S. Terekhov, O. P. Sushkov, *2D Mater.* **2**, 014010 (2015).
 - ¹⁴ M. Haze, Hung-Hsiang Yang, K. Asakawa, N. Watanabe, R. Yamamoto, Y. Yoshida, and Y. Hasegawa, *Rev. Sci. Instrum.* **90**, 013704 (2019).
 - ¹⁵ H. Kim, A. Palacio-Morales, T. Posske, L. Rzsa, K. Palots, L. Szunyogh, M. Thorwart and R. Wiesendanger, *Sci. Adv.* **4**, eaar5251 (2018).
 - ¹⁶ C. Friesen, H. Osterhage, J. Friedlein, A. Schlenhoff, R. Wiesendanger, S. Krause, *Science* **363**, 1065 (2019).
 - ¹⁷ F. D. M. Haldane, *Phys. Lett. A* **93**, 464 (1983); *Phys. Rev. Lett.* **50**, 1153 (1983).
 - ¹⁸ T. Kennedy, *J. Phys. Condens.: Matter* **2**, 5737 (1990).
 - ¹⁹ V. N. Kotov, O. P. Sushkov, R. Eder, *Phys. Rev. B* **59**, 6266 (1999).
 - ²⁰ P. V. Shevchenko, A. W. Sandvik, O. P. Sushkov, *Phys. Rev. B* **61**, 3475 (2000).
 - ²¹ T. B. Boykin, G. Klimeck, M. A. Eriksson, M. Friesen, S. N. Coppersmith, P. von Allmen, F. Oyafuso, and S. Lee, *Appl. Phys. Lett.* **84**, 115 (2004).
 - ²² V. L. Campo, Jr., and M. Cococcioni, *J. Phys. Condens. Matter* **22**, 055602 (2010).
 - ²³ P. W. Anderson, *Phys. Rev.* **79**, 350 (1950).
 - ²⁴ S. Sachdev, and R. N. Bhatt, *Phys. Rev. B* **41**, 9323 (1990).
 - ²⁵ K. Takatsu, W. Shiramura, and H. Tanaka, *J. Phys. Soc. Jpn.* **66**, 1611 (1997).
 - ²⁶ P. Merchant, B. Normand, K. W. Krmer, M. Boehm, D. F. McMorrow, and Ch. Rüegg, *Nat. Phys.* **10**, 373 (2014).